Shape Estimation of a 3D Printed Soft Sensor Using Multi-Hypothesis Extended Kalman Filter

Kaige Tan, *Member, IEEE*, Qinglei Ji, Lei Feng, *Member, IEEE*, and Martin Törngren, *Senior Member, IEEE*

***Abstract*—This study develops a multi-hypothesis extended Kalman filter (MH-EKF) for the online estimation of the bending angle of a 3D printed soft sensor attached to soft actuators. Despite the advantage of compliance and low interference, the 3D printed soft sensor is susceptible to the hysteresis property and nonlinear effects. Improving measurement accuracy for sensors with hysteresis is a common challenge. Current studies mainly apply complex models and highly nonlinear functions to characterize the hysteresis, requiring a complicated parameter identification process and challenging real-time applications. This study enhances the model simplicity and the real-time performance for the hysteresis characterization. We identify the hysteresis by combining multiple polynomial functions and improving the sensor estimation with the proposed MH-EKF. We examine the performance of the filter in the real-time closed-loop control system. Compared with the baseline methods, the proposed approach shows improvements in the estimation accuracy with low computational complexity.**

***Index Terms*—Soft Sensors and Actuators, Modeling, Control, and Learning for Soft Robots, Hydraulic/Pneumatic Actuators.**

I. Introduction

SOFT robots are made from compliant materials and outperform conventional rigid robots in terms of adaptability, safety, and novel actuation [1]. Soft robots move and interact with the environment through the soft actuators, which deform by morphing their soft bodies. However, due to the compliant nature of the flexible materials, soft actuators also suffer from low actuation precision and long response time, which hinders their wider applications [2], [3].

Integrating shape or force sensors onto the soft actuators to provide signal feedback is a natural solution to increase the actuator performance [4]. 3D printing, a powerful and versatile additive manufacturing technology for producing complex and multi-material structures, has been intensively applied in fabricating soft actuators directly integrated with printed soft sensors [5]. These printed soft sensors either use commercial conductive filaments [6] or self-developed materials [7] that exhibit deformation responsive properties. The feedback from the sensors is usually the resistance or capacitance, which can be measured to predict the deformed shape using the shape estimation model for the sensor readings and the sensor shape.

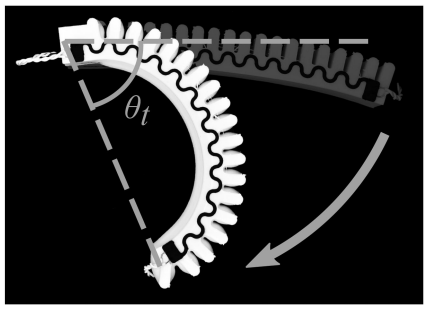

Fig. 1. The 3D printed soft actuator with integrated soft sensor. The soft actuator is deformed with the bending angle θ_t.

However, the hysteresis phenomena widely exist in the piezoresistive materials [8]–[10], causing the measurement inconsistency when the sensor is deformed and recovered [11]. As a result, the soft sensors suffer from large uncertainties and measurement errors. In our previous work [12], we developed a strain sensor that can be directly 3D printed on a bellow-type soft actuator as shown in Fig. 1. The sensor is printed using a flexible conductive filament, and its electric resistance changes when deformed with the soft actuator. By measuring the real-time resistance, the shape of the soft actuator is estimated using a linear resistance-deformation model. The estimated actuator shape then enables closed-loop shape control of the soft actuator. However, the controller performance varies for different shape references without considering the hysteresis in the shape estimation model. A shape estimation model that tackles the influence of the hysteresis is required.

Currently, to characterize the hysteresis behavior and compensate for its negative effect, phenomenological models that express the experimental phenomenon with the relevant mathematical model [13]–[15] are extensively applied. In addition, operator-based models, including Preisach model [16] and Prandtl-Ishlinskii (PI) model [17], employ the combination of multiple weighted play operators. By this means, hysteresis is modeled as a cumulative effect of all possible delayed relay

Manuscript received 1 March 2022; accepted 20 June 2022. Date of publication 1 July 2022; date of current version 11 July 2022. This letter was recommended for publication by Associate Editor P. Chirarattananon and Editor Y.-L. Park upon evaluation of the reviewers' comments. This work was supported by the TECoSA Vinnova Competence Center for Trustworthy Edge Computing Systems and Applications at KTH Royal Institute of Technology and in addition been partly supported through the InSecTT. InSecTT has received funding from the ECSEL Joint Undertaking (JU) under Grant agreement No 876038. *(Corresponding author: Lei Feng.)*

Kaige Tan, Lei Feng, and Martin Törngren are with the Department of Machine Design, KTH Royal Institute of Technology, 10044 Stockholm, Sweden (e-mail: kaiget@kth.se; lfeng@kth.se; martint@kth.se).

Qinglei Ji is with the Department of Production Engineering and Department of Machine Design, KTH Royal Institute of Technology, 10044 Stockholm, Sweden (e-mail: qinglei@kth.se).

This letter has supplementary downloadable material available at https://doi.org/10.1109/LRA.2022.3187832, provided by the authors.

Digital Object Identifier 10.1109/LRA.2022.3187832

elements parameterized by a pair of threshold variables [18]. Studies on hysteresis modeling also exploit data-driven methods. The hysteresis property is analyzed by the Gaussian Process in [19], where the control signal and its corresponding changing rate are taken as the model input. The Duhem model is transformed to a neural network model in [20] to describe hysteresis and perform parameter identification.

The above-mentioned approaches essentially utilize domain-specific models or highly-nonlinear basis functions to construct a complex relationship to characterize the hysteresis, which requires a complicated parameter identification process. With the increase of parameters, advanced identification methods (e.g., searching and optimization-based methods [21]–[23]) are required to calibrate the model, which has low efficiency and a non-negligible risk of falling into local minimal. A modeling approach that features low complexity and high accuracy is required, so that the algorithm can be implemented in a microcontroller for real-time control.

Based on our previous findings [12], this study investigates Kalman filter (KF) to improve the shape estimation. In particular, to characterize the hysteresis property, a set of quadratic functions are approximated to differentiate the angle increasing and decreasing phases under different amplitudes. Moreover, a multi-hypothesis Extended Kalman Filter (MH-EKF) is designed to improve the sensor performance with high accuracy and efficiency. MH-EKF enhances the KF by evaluating posterior probabilities of all feasible association hypotheses [24], which has been widely used in the localization [25], [26] and tracking problems [27], [28] in the field of mobile robots and vehicles. In this study, we extend its usage and investigate the application in the soft sensor hysteresis problem. For validation, the developed method is implemented on a microcontroller for the closed-loop control to test the precision and real-time performance.

The rest of this letter is organized as follows. In Section II, we give a brief overview of the experiment setup, followed by the identification of the actuator's dynamic model and the pressure-angle hysteresis. Section III describes the design of the KF and MH-EKF approaches. The performance of the filters with the real-time implementation is tested in Section IV. Section V concludes this study.

II. Model Identification

A. Experiment Setup

The soft sensor is printed onto the soft actuator directly via multi-material 3D printing methods. The soft actuator is printed with thermoplastic polyurethane (TPU) and the soft sensor is printed with EEL, which is a mixture of TPU and carbon black. Its electric resistance is deformation-responsive owing to the changed distribution of carbon black during deformation. The influences of different sensor shapes on the sensor performance were investigated in an earlier study [12], and the sine wave shape applied in this work is found to be the optimal profile. Fig. 2 gives an overview of the test rig for the soft sensor characterization and soft actuator control. The soft actuator deformation is produced by the air pressure from the pressure regulator, which is connected to a pressure source of 6 bar. The regulator is controlled by an Arduino Due microcontroller board. The pressure regulator is assumed to be an ideal regulator and provides pressure output equal to the pressure reference with no delay. A MATLAB Simulink program runs on the computer and downloads the compiled program to the microcontroller board. The program also communicates with the board in real-time to monitor the system status and send commands.

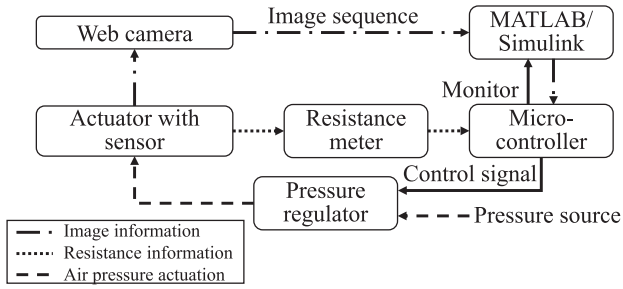

Fig. 2. Overview of the experiment setup.

Under the constant curvature assumption, the deformed soft actuator is an arc [3]. The deformation of the actuator can be expressed using the bending angle θ_t, which refers to the angle formed by the arc, as illustrated in Fig. 1. Due to the residual stress from 3D printing the soft actuator, the initial shape is not straight and the actuator has a free bending angle of $\theta_0 = 18^\circ$. In the later context, this initial angle is subtracted from θ_t. Thus, θ_t refers to the varied bending angle. Two methods are used to detect the bending angle. First, a web camera is used to capture the bending angle in real-time with the designed image feedback module [3]. The bending angle captured by the camera is regarded as the ground truth, which is used both in model identification and the closed-loop validation. The camera angle value is sent to the board via serial communication. In addition, a resistance meter circuit connecting the sensor on the soft actuator is applied and converts the varied electric resistance during deformation to analog signals, which is then measured by the microcontroller board as the digital resistance reading [12].

B. Motion Model

A state-space model is required to find the relationship between the input pressure and the actuator's bending angle. Several studies have addressed the actuator modeling, such as Finite Element Modeling (FEM) [29] and data-driven methods [30]. A data-driven linear model is investigated in the prior study [3] and shows adequate accuracy. Therefore, we continue to use a linear identified model. In particular, we record the bending angle θ with time stamps t by exciting the soft actuator with a series of air pressure ranging from $1 \sim 3\ bar$ with the increment of $0.25\ bar$ in each experiment. The soft actuator can reach a steady bending angle θ_∞ within 1.5 s. Fig. 3(a) depicts the relation of θ_∞ against P, and it can be expressed by $\theta_\infty = 18.1P$. The estimation accuracy is evaluated by the coefficient of determination denoted by R^2 [31]. The fitting model has $R^2 = 95.2\%$, showing that the actuator response can be approximated to a linear model and the steady-state gain is 18.1. Fig. 3(b) plots the dynamic

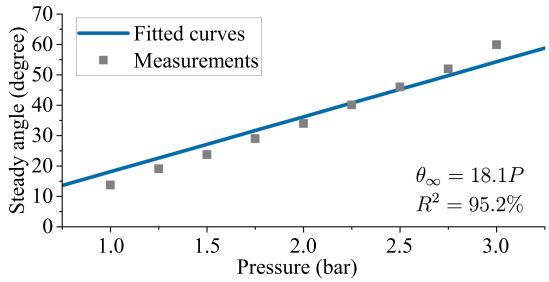

(a) Steady angle versus input pressure.

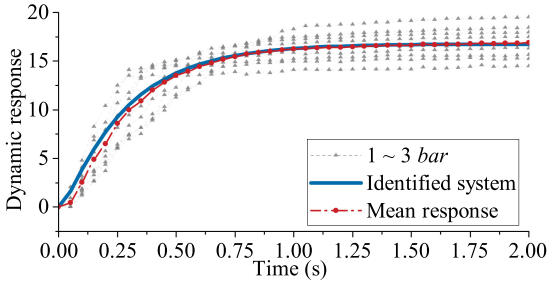

(b) Actuator dynamic response versus time.

Fig. 3. State transition model fitting for the soft actuator.

responses under different stimuli. Subsequently, the system behavior is concluded by fitting the average responses with the unit input pressure. Owing to the low complexity and high precision, we apply *ssest* function in MATLAB and generate a second-order discrete-time state-space model with the sampling time $T_s = 50\,\text{ms}$, given as

$$\mathbf{x}_{t+1} = A_{\text{dis}}\mathbf{x}_t + B_{\text{dis}}P_t, \tag{1a}$$

$$\theta_t = C^0_{\text{dis}}\mathbf{x}_t = [1 \quad 0]\mathbf{x}_t, \tag{1b}$$

where $\mathbf{x}_t = [\theta_t \quad \dot{\theta}_t - N_1 P]^\top$ is a 2×1 state vector. The controllability and observability can be verified by checking that the matrices $\mathcal{C} = \begin{bmatrix} B_{\text{dis}} & A_{\text{dis}}B_{\text{dis}} \end{bmatrix}$ and $\mathcal{O} = \begin{bmatrix} C^0_{\text{dis}} \\ C^0_{\text{dis}}A_{\text{dis}} \end{bmatrix}$ have the full rank. The step response of the approximated model is shown in Fig. 3(b). Compared to the experimental data, the identified system through approximation is accurate in terms of rise time and steady-state error ($R^2 = 98.29\%$).

C. Observation Model

In a real-time application, the output matrix $C^0_{\text{dis}} = [1 \quad 0]$ in (1b) cannot be applied directly since the bending angle is not directly measured. As mentioned before, we apply the soft sensor attached to the actuator, where bending angles can be detected with resistance readings of the soft sensor. The resistance measurement at time-t is converted to the digital reading of the microcontroller as the measurement variable, denoted by r_t. In the previous solution [12], a linear regression model builds the observation relationship with

$$\theta_t = Kr_t, \tag{2}$$

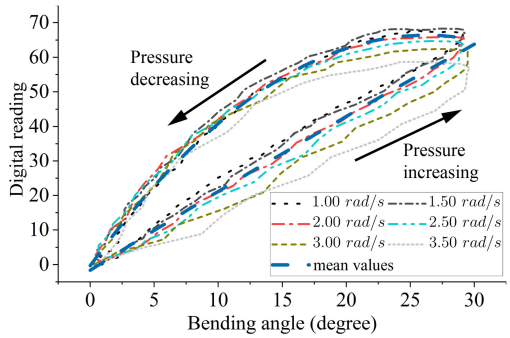

(a) Bending angle versus normalized digital resistance reading, with the varied frequencies and identical amplitude.

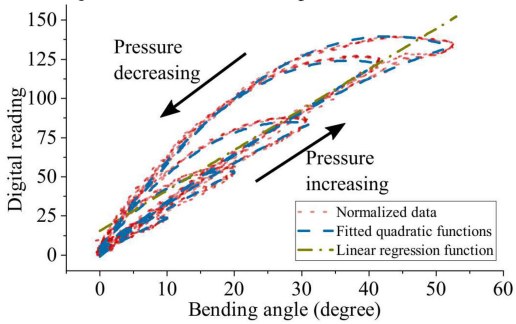

(b) Bending angle versus normalized digital resistance reading, with the varied amplitudes and identical frequency.

Fig. 4. Hysteresis loops generated by the soft sensor. Arrows represent the pressure increasing and decreasing phases.

where K is a constant estimated from the collected data. Based on (2), we can rewrite the state-space expression in (1b) as

$$\hat{r}_t = C_{\text{dis}}\mathbf{x}_t, \tag{3}$$

where $C_{\text{dis}} = [K^{-1} \quad 0]$. We denote $\hat{r}_t$ as the prediction to distinguish the real measurement r_t. Note that K is non-zero, which ensures the feasibility of (3).

The linear regression is efficient but also causes model inaccuracy. Due to the hysteresis, a specific bending angle can map to different resistance readings. Fig. 4(a) illustrates the hysteresis property of the applied soft sensor, where the digital readings vary during the pressure increasing and decreasing phases. The data is collected by driving the soft actuator with a sine wave. Note that the origin of the hysteresis loop is shifted to zero in the figures. Specifically, we compare the hysteresis behaviors in Fig. 4(a) when imposing pressure inputs with different frequencies but the identical amplitude. Although small variances in the shapes of hysteresis loops appear, the measurements under different frequencies have a similar behavior. To simplify the model, we assume that the hysteresis in the applied soft sensor holds the rate-independent property [8], because the shapes of the hysteresis loops have little correlation with the rate of the input signal. In addition, as seen in Fig. 4(b), when driving the soft actuator with different amplitudes but a fixed frequency, the hysteresis loops manifest different patterns, especially during the angle decreasing stage. If the linear approximation is used to estimate the bending angle from the resistance reading, the estimation error would be large. To improve the accuracy,

the relationship between the bending angle and the resistance must adapt to different amplitudes and the increasing/decreasing phases. This motivates us to find multiple polynomial approximations to characterize the hysteresis loops.

In particular, we denote a set of quadratic functions by $f_i(\theta) = a_i\theta^2 + b_i\theta + c_i,\ i \in \mathcal{I}$, to characterize the hysteresis during the angle increasing/decreasing process. In this study, we limit the operational range of the soft actuator from 10° to 50°. The collected data with different amplitudes of bending angles are applied separately for polynomial curve fitting. To avoid high-frequency measurement noises, the original data are pre-processed by a moving average filter [32] with the window size of 10. The fitted quadratic functions are depicted in Fig. 4(b), where the linear regression result is also given for comparison, which is fitted with the 50° hysteresis loop data. The fitted quadratic functions have an average R^2 value of 98.46%. For the linear regression function, the corresponding coefficient of determination is $R^2 = 89.88\%$. The quadratic function is selected due to simplicity and precision. Notice that the hysteresis loop does not exhibit a high level of non-linearity by checking the second-order derivative being small. Thus, the extended Kalman filter approach is suitable to be applied, in which the accuracy can be preserved by linearizing the quadratic measurement functions.

III. Design of Filters

In this section, the Kalman filter approach is developed to obtain high-accuracy sensor shape estimations. We treat the approximation error together with the environmental noise as Gaussian. Due to the inherent non-linearity and multi-modality from the hysteresis loop, we identify the measurement model by proposing an MH-EKF approach.

A. The Kalman Filter

In the Kalman filter, the state is represented by the posterior probabilities based on the past measurements and controls [33]. Therefore, from (1) and (3), we can rewrite the linear Gaussian state transition equations with

$$\mathbf{x}_{t+1} = A_{\text{dis}}\mathbf{x}_t + B_{\text{dis}}P_t + \boldsymbol{\epsilon}, \tag{4a}$$

$$r_t = C_{\text{dis}}\mathbf{x}_t + \delta. \tag{4b}$$

The two terms $\boldsymbol{\epsilon} \in \mathbb{R}^2$ and $\delta \in \mathbb{R}$ are state transition and measurement noises, respectively. Both are Gaussian with the constant covariance matrices R and Q.

The Kalman filter algorithm represents the state probability $p(\mathbf{x}_t) \sim \mathcal{N}(\mathbf{x}_t; \boldsymbol{\mu}_t, \Sigma_t)$ by the mean $\boldsymbol{\mu}_t$ and the covariance Σ_t. Given the posterior at time $t-1$, the prediction of the state $p(\bar{\mathbf{x}}_t) \sim \mathcal{N}(\bar{\mathbf{x}}_t; \bar{\boldsymbol{\mu}}_t, \bar{\Sigma}_t)$ is calculated as

$$\bar{\boldsymbol{\mu}}_t = A_{\text{dis}}\boldsymbol{\mu}_{t-1} + B_{\text{dis}}P_{t-1}, \tag{5a}$$

$$\bar{\Sigma}_t = A_{\text{dis}}\Sigma_{t-1}A_{\text{dis}}^\top + R. \tag{5b}$$

Then, by incorporating a linear measurement model, the posterior of the state $\mathbf{x}_t$ is updated with

$$\boldsymbol{\mu}_t = \bar{\boldsymbol{\mu}}_t + K_t(r_t - C_{\text{dis}}\bar{\boldsymbol{\mu}}_t), \tag{6a}$$

$$\Sigma_t = \bar{\Sigma}_t - K_t C_{\text{dis}}\bar{\Sigma}_t, \tag{6b}$$

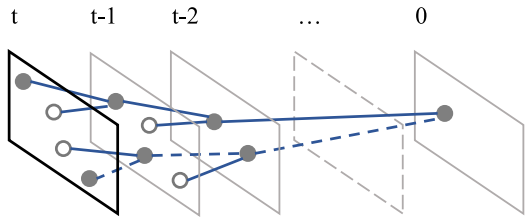

Fig. 5. Illustration of tracks in the MH-EKF.

where K_t is the Kalman gain, which is calculated as

$$K_t = \bar{\Sigma}_t C_{\text{dis}}^\top \left(C_{\text{dis}}\bar{\Sigma}_t C_{\text{dis}}^\top + Q\right)^{-1}. \tag{7}$$

B. Multi-Hypothesis Extended Kalman Filter

The hysteresis property complicates the Kalman filter by introducing the non-linear and multi-modal beliefs. Thus, the MH-EKF is applied to represent the posterior by multiple Gaussians. As discussed in Section II-C, we describe the hysteresis loop with the quadratic functions; hence, the measurement from a specific quadratic function f_i is governed by

$$r_t^i = h_i(\bar{\mathbf{x}}_t) + \delta_t^i, i \in \mathcal{I}, \tag{8}$$

where $h_i : \mathbb{R}^2 \to \mathbb{R}$, and $h_i(\mathbf{x}_t) := f_i(C_{\text{dis}}^0\mathbf{x}_t) = f_i(\theta_t)$ is one of the hypotheses in the observation model. In the EKF, the measurement model is approximated by the first-order Taylor expansion around $\bar{\boldsymbol{\mu}}_t$, which gives

$$h_i(\mathbf{x}_t) \approx h_i(\bar{\boldsymbol{\mu}}_t) + H_t^i(\mathbf{x}_t - \bar{\boldsymbol{\mu}}_t). \tag{9}$$

H_t^i is the corresponding Jacobian matrix, and $H_t^i = \begin{bmatrix} \frac{df_i}{d\theta_t} & 0 \end{bmatrix} = \begin{bmatrix} 2a_i\bar{\theta}_t + b_i & 0 \end{bmatrix}$, where $\bar{\theta}_t$ is the first entry in $\bar{\boldsymbol{\mu}}_t$.

With a certain measurement model h_i, the posterior for EKF $p(\mathbf{x}_t^i) \sim \mathcal{N}\left(\mathbf{x}_t^i; \boldsymbol{\mu}_t^i, \Sigma_t^i\right)$ is updated by

$$\boldsymbol{\mu}_t^i = \bar{\boldsymbol{\mu}}_t + K_t^i(r_t - h_i(\bar{\boldsymbol{\mu}}_t)), \tag{10a}$$

$$\Sigma_t^i = \bar{\Sigma}_t - K_t^i H_t^i \bar{\Sigma}_t, \tag{10b}$$

where $K_t^i = \bar{\Sigma}_t H_t^{i\top}\left(H_t^i\bar{\Sigma}_t H_t^{i\top} + Q\right)^{-1}$. Note that $\bar{\Sigma}_t$ is unchanged because the state update equation is still described by the linear equation (4a).

As an extension of the basic EKF, MH-EKF accepts multiple hypotheses in the belief. It represents the posterior by combining closely related hypotheses [33]. Fig. 5 gives an illustration of the MH-EKF. The example contains two hypotheses in the measurement model (i.e., $|\mathcal{I}| = 2$), which are depicted by the nodes generated at each time step. We denote a node at time-t by $l_t \in \mathcal{I}$, and it represents the measurement model that a hypothesis selects. A Gaussian path is extended with new nodes by selecting measurement models at different times, which is represented by the dashed line in Fig. 5. This process generates a tree whose root is at $t = 0$ and the sequence length is $t+1$. We denote the set of all Gaussian paths by $\mathcal{L} \subseteq \mathcal{I}^*$, and a path from time 0 to time t by $l[t] = l_0 l_1 \ldots l_t \in \mathcal{L}$. A path $l[t]$ from the root to a node at time-t is uniquely defined by specifying the hypothesis correspondence on the measurement model during the period $[0, t]$.

In Fig. 5, the grey nodes represent the valid paths that can propagate to the next time step, and the empty nodes are paths that are terminated. In the MH-EKF, since new hypotheses are generated at each time step, the new nodes grow exponentially over time. For this reason, the number of Gaussian paths should be limited. To overcome this issue, two methods are applied in this study. First, we define a threshold $\bar{D}_{\mathrm{M}}$ on Mahalanobis distance to filter out the hypotheses with low measurement likelihood. The Mahalanobis distance D_i estimates the likelihood by calculating the distance between the measurement and the probability distribution of a hypothesis. It is given by

$$D_i = (r_t - h_i(\bar{\mathbf{x}}_t))^2 \left(H_t^i \bar{\Sigma}_t H_t^{i\top} + Q\right)^{-1}, i \in \mathcal{I}. \tag{11}$$

Second, we define an upper limit on the number of valid paths by $\bar{N}$, i.e., $|\mathcal{L}| \leq \bar{N}$. We perform the pruning by only selecting the top $\bar{N}$ paths with higher weights. The definition of the path weight $\psi^{l[t]}$ is given later in (13) and (14). By these means, we eliminate redundant computation, which benefits our real-time implementation.

The posterior $\mathbf{x}_t$ in MH-EKF depends on all valid paths in $\mathcal{L}$ at time-t. Each path can be viewed as the local posterior function $\mathbf{x}^{l[t]}$ conditioned on a unique sequence of measurement model associations, and is defined by a Gaussian with mean $\boldsymbol{\mu}^{l[t]} = \boldsymbol{\mu}_t^{l_t}$ and covariance $\Sigma^{l[t]} = \Sigma_t^{l_t}$ based on (10). By associating the paths, the expected posterior at time-t is $p(\mathbf{x}_t) \sim \mathcal{N}(\mathbf{x}_t; \boldsymbol{\mu}_t, \Sigma_t)$, characterized by

$$\boldsymbol{\mu}_t = \frac{1}{\sum_{l[t]} \psi^{l[t]}} \sum_{l[t]} \psi^{l[t]} \boldsymbol{\mu}^{l[t]}, \tag{12a}$$

$$\Sigma_t = \frac{1}{\left(\sum_{l[t]} \psi^{l[t]}\right)^2} \sum_{l[t]} \left(\psi^{l[t]}\right)^2 \Sigma^{l[t]}, \tag{12b}$$

where $\psi^{l[t]} > 0$ is the path weight, which determines the weight of path-$l[t]$ in the posterior. The weight $\psi^{l[t]}$ is updated at each time step. Assume that a path $l[t-1]$ has the weight $\psi^{l[t-1]}$. It propagates to a new path $l[t]$ by the hypothesis correspondence $l_t = i$. Then, the weight of the new path-$l[t]$ is calculated as

$$\hat{\psi}^{l[t]} = \psi^{l[t-1]} p(r_t \mid l[t-1] \circ l_t), \ \ i \in \mathcal{I}, \tag{13}$$

where the operator $\circ$ denotes a connection function that associates $l[t-1]$ and l_t. $\hat{\psi}^{l[t]}$ denotes the path weight before normalization. Note that $\psi^{l[t]}$ is obtained after normalization to avoid the weight attenuation, and is given by

$$\psi^{l[t]} = \hat{\psi}^{l[t]} / \sum\nolimits_{l[t]} \hat{\psi}^{l[t]}. \tag{14}$$

The term $p(r_t \,|\, l[t-1] \circ l_t)$ in (13) is the likelihood of the measurement r_t under the sequence of correspondence (i.e., $l[t-1] \circ l_t$) that leads to the new path $l[t]$ from $l[t-1]$. It follows the Gaussian distribution with the form [33]

$$p(r_t \mid l[t-1] \circ l_t) \sim \mathcal{N}\left(r_t; h_i(\bar{\boldsymbol{\mu}}_t), H_t^i \bar{\Sigma}_t H_t^{i\top} + Q\right). \tag{15}$$

(13) gives an overall estimation on a new path $l[t]$ by both considering the measurement likelihood at the current time-t (i.e., $p(r_t \,|\, l[t-1] \circ l_t)$), and the weight of the path it inherits (i.e., $\psi^{l[t-1]}$).

Algorithm 1: Multi-hypothesis-based EKF.

Data: State transition covariance matrix R, measurement variance Q, Mahalanobis distance threshold $\bar{D}_{\mathrm{M}}$, track threshold $\bar{N}$
Result: Gaussian mixture posterior $p(\mathbf{x}_t)$

```
Initialize μ_0 = [0 0]^⊤, Σ_0 = Σ_init, t = 1, L' = {ϵ};
while t ≤ T do
    L = ∅;
    foreach l[t-1] ∈ L' do
        Obtain p(x̄_t) by (5);
        Receive measurement r_t;
        foreach i ∈ I do
            Build a new path-l[t] with l_t = i and the
              sequence of correspondence
              l[t] ← l[t-1] ∘ l_t;
            Obtain p(x_t^i), D_i from (10), (11);
            if D_i ≤ D̄_M then
                Obtain p(r_t | l[t-1] ∘ l_t) from (15);
                Update ψ̂^{l[t]} from (13);
                Append the element: L ← L ∪ {l[t]};
            end
        end
    end
    Perform pruning of L based on N̄;
    Normalize weight from (14);
    Obtain the posterior p(x_t) from (12);
    Update Gaussian path set: L' ← L;
    Update time step: t ← t + 1;
end
```

Algorithm 1 presents the pseudo-code for the MH-EKF implementation during the period $[0, T]$. Note that two sets, i.e., $\mathcal{L}'$ and $\mathcal{L}$, are defined to store the paths from the last time step and the updated paths at the new time step. The initial set of $\mathcal{L}'$ contains only the empty path ϵ, which represents the root node of all hypothesis paths. The initial value of Σ_0 is a tuning parameter, which is fine-tuned during the experiments. The associated computation complexity at each time step is $\mathcal{O}(|\mathcal{L}'||\mathcal{I}|)$, which is at most $\mathcal{O}(\bar{N}|\mathcal{I}|)$ and linear in the number of hypotheses. It indicates that the method is scalable to a large-scale problem when extending the operational range of the soft actuator and incorporating more hypotheses in the observation model. In addition, since the EKF estimation of each hypothesis can be computed independently, the runtime has the potential of being largely reduced by parallel computing.

IV. Experiments and Results

To evaluate the accuracy of the MH-EKF approach, we compare its performance against the following methods.

1) **Linear Regression (LR)**: The bending angle θ_t is estimated by the measurement r_t through (2).
2) **Kalman Filter (KF)**: The estimation $\hat{r}_t$ is calculated through (3) with the linear observation model.

The bending angle θ_t is also captured by a web camera and analyzed by image processing, and the value from Camera Angle (CA) is regarded as the ground truth to be compared with. LR is

TABLE I
PARAMETER VALUE SELECTION

Parameter	Value
State transition covariance matrix, R	$20I_2$
Measurement variance, Q	100
Threshold on Mahalanobis distance, $\bar{D}_{\mathrm{M}}$	1
Threshold on valid tracks, $\bar{N}$	3
Number of hypothesis, $\lvert\mathcal{I}\rvert$	10

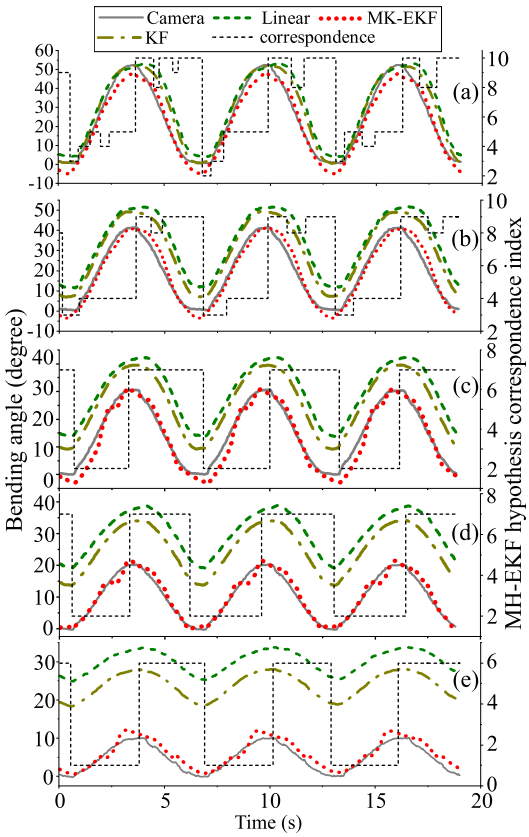

Fig. 6. Angle estimation comparison and MH-EKF hypothesis correspondence index result. The input is a sine wave with the frequency of 1 rad/s. The amplitudes are varied, where (a)∼(e) corresponds to $50^\circ \sim 10^\circ$ with the step of 10°.

applied in the prior works [12], which is viewed as the baseline for comparison. In KF, the measurement estimation uses the same linear relationship as in LR. The parameter setting can be found in Table I. I_2 denotes the identity matrix of size 2.

A. Estimation Comparisons

First, as shown in Fig. 6, we compare the accuracy of angle estimation by driving the soft actuator with periodical sine waves of different angle amplitudes. In Fig. 6(a), the maximal amplitude is set to 50°, which is the same as used for the linear regression fitting. Thus, all three methods can follow the ground-truth signal with high accuracy. MH-EKF outperforms the other two slightly in the angle decreasing half period because both KF and LR methods adopt a linear observation model, and the high-precision approximation can only be guaranteed on the one side of the hysteresis loop. This leads to the asymmetry in estimation accuracy, and the performance is worse in the angle

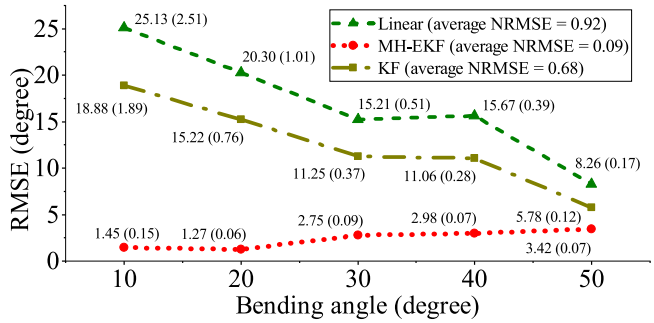

Fig. 7. Comparison of the RMSE of different estimation methods. The values of NRMSE are given in parentheses.

decreasing phase. Note that all three methods can finish the estimation workload on the microcontroller within one control period, which shows the feasibility of MH-EKF in the real-time application.

In Fig. 6(b)∼(e), when the amplitude decreases, both KF and LR show significant performance deterioration gradually. It can be inferred from Fig. 4(b) that the hysteresis loop changes its shape with different input signals. Therefore, the linear assumption loses its accuracy, especially when the amplitude deviates more from the curve-fitting one. Nevertheless, MH-EKF can follow the actual bending angle by collaborating multiple hypotheses. It maintains a high precision by adapting the weights for hypotheses under different situations.

We also show the MH-EKF hypothesis correspondence result in Fig. 6, where only the hypothesis with the highest weight is selected and plotted. As $|\mathcal{I}| = 10$, the range of the index is $1 \sim 10$. Note that the indices $1 \sim 5$ represent the $10^\circ \sim 50^\circ$ amplitude hypotheses on the angle increasing phase, while $6 \sim 10$ correspond to the angle decreasing phase. The results verify the correctness of the correspondence in MH-EKF, although slight oscillations and errors can be noticed in the 40° and 50° scenarios. We regard this as part of future work to improve and increase estimation robustness.

We plot the estimation accuracy in Fig. 7 by comparing the root-mean-square error (RMSE) under different situations. The RMSE is further normalized by the range of the measured data to get the normalized RMSE (NRMSE). Similar to Fig. 6, the error ascends in both LR and KF with lower amplitudes. Meanwhile, MH-EKF witnesses an increasing trend with larger angles but still keeps the estimation error at a low level. Besides, the NRMSE of MH-EKF remains stable across the range of bending angles. The larger estimation errors of LR and KF when the amplitude decreases can be attributed to the selected linearized point in the measurement model. As mentioned in Section II-C, the linear measurement model is approximated with the 50° hysteresis loop data. Thus, both LR and KF have their least approximation errors in the 50° amplitude scenario, but the inaccuracies increase for smaller bending angles. It can be seen that LR has the largest error with an average NRMSE of 0.92, while MH-EKF outperforms the others significantly with an average NRMSE of 0.09.

Fig. 8 plots the hysteresis loop in the 50° and 20° scenarios, respectively. Compared to the ground truth signal, MH-EKF

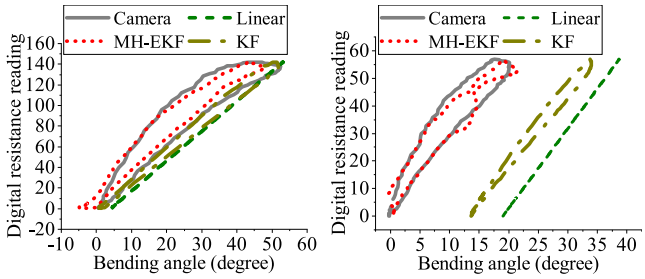

(a) Hysteresis loops at 50°. (b) Hysteresis loops at 20°.

Fig. 8. Comparison of the hysteresis loop estimations in the 50° and 20° scenario.

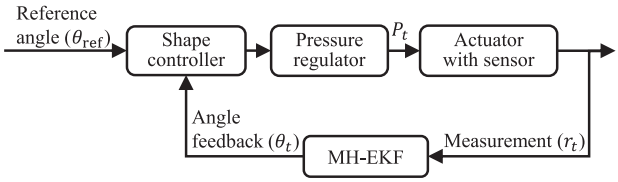

Fig. 9. Closed-loop control structure.

identifies the real hysteresis loop more accurately than LR and KF in both scenarios. Both LR and KF approximate more closely in the 50° scenario as it is used for the curve-fitting, but leave a large gap in the 20° scenario, where the drawback of the linear model is revealed. The angle estimation is not correct when provided with the same digital resistance reading, as it can also be observed in Fig. 6(d). Although much better than LR and KF, MH-EKF displays larger errors in Fig. 8(b) when the bending angle is close to the peak value of 20 degrees. The errors are also visible in Fig. 6(d). Improvements in the estimation accuracy for the small bending angle scenario will be studied.

The computation efficiency is critical for the real-time filtering performance. The estimation period in this case is defined as identical to the sampling time of the discrete state-space motion model with 50 ms. The microcontroller board is featured by 84 MHz clock speed, 96 KB SRAM, and 512 KB flash memory[1]. The onboard execution times of the estimation algorithms are measured by profiling tools[2]. In one sampling period, the average computation time is 0.008, 0.119, and 3.507 ms for LR, KF, and MH-EKF, respectively. The LR only performs a linear calculation; thus, its computation time is the shortest. Note that, although the MH-EKF takes more computation time than its counterparts, its average CPU utilization is only 7.01%, and it improves the estimation accuracy significantly. Therefore, the proposed method has a fair computational complexity and better numerical accuracy.

B. Closed-Loop Control Applications

We validate the estimation performance of the MH-EKF in the closed-loop control system. Fig. 9 shows the closed-loop control structure. The input signal is the reference angle θ_{ref}, followed by a feedforward and error feedback PI controller for the shape control of the soft actuator. The reference signal is compared with the angle feedback from the MH-EKF, and the angle deviation is sent into the PI controller to derive the input pressure P_t. The pressure signal generated by the output feedback control is expressed as

$$P_t = K_{\text{ff}}\theta_{\text{ref}} + K_p(\theta_{\text{ref}} - \theta_t) + K_i \int (\theta_{\text{ref}} - \theta_t)dt, \qquad (16)$$

where $K_{\text{ff}}\theta_{\text{ref}}$ is the feed forward part. The value of K_{ff} is given based on the identified model. We assign its value with the steady-state gain that is derived in Section II-B, and $K_{\text{ff}} = 18.1$. The rest part in (16) is the error feedback part and a PI controller is deployed. The parameters in the PI controller are pre-defined with aid of the system model and then fine tuned with experimental methods. Since it is not the focus of this work, the details of the controller design is omitted and can be found in [12].

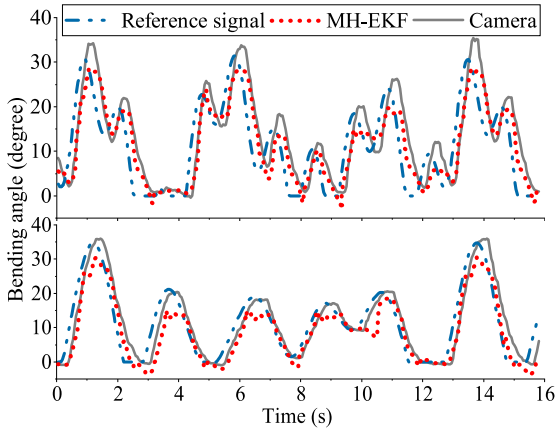

Fig. 10. Comparison of the closed-loop shape control performance with the MH-EKF signal as feedback.

To test the performance in a generalized scenario, we design two random angle reference signals composed of multiple sine waves of various amplitudes, frequencies, and phases. The angle references are expressed as $\theta_{\text{ref}} = \frac{1}{N}\sum_{i=1}^{N}[A_i \sin(2\pi f_i + \phi_i)]$, where $N = 5$, $A_i \in [10, 50]$, $f_i \in [1, 4]$, $\phi_i \in [0, 3]$.

In Fig. 10, the control performance is validated when taking the MH-EKF estimation as feedback, and the results for two reference signals are shown separately in subfigures. Despite the delay in the closed-loop control, MH-EKF can keep track of the reference angle with relatively high accuracy. Compared to the camera angle as the ground truth, it has the maximal estimation errors of 7.74° and 8.73° in two scenarios. The NRMSE values are 0.07 and 0.09, respectively. The NRMSE results are consistent with the observations from the sine wave experiments. The deviation between Camera and MH-EKF becomes more prominent at peaks of the time series, which follows the trend in Fig. 6∼7. The maximal error is larger than that in the sinewave test, mainly due to the irregular angle change with random references. The applied state-space model loses accuracy in such scenarios, and we regard it as one part of future works to be improved.

[1]https://docs.arduino.cc/hardware/due

[2]https://se.mathworks.com/help/supportpkg/arduino/ref/code-execution-profiling-for-arduino-hardware-in-external-mode.html

V. Conclusion and Future Work

This study investigates the Kalman filter usage in the 3D printed soft sensor application. The linear estimation method in the prior study has limitations due to the hysteresis property in the soft sensor. To overcome this problem, we analyze the hysteresis loop with multi-modal assumptions and realize the accurate observation model with multiple quadratic functions. In addition, the MH-EKF method is proposed to improve the sensing performance while guaranteeing real-time computation efficiency. A more precise bending angle estimation is reached in the closed-loop control system. We compare the performance of MH-EKF with the Kalman filter and the linear regression method. The experimental results verify that our approach outperforms the baseline methods by decreasing the average NRMSE from 0.92 to 0.09.

The future work will be investigated in three directions. First, the prediction model can be identified with higher complexity. The state-space can be augmented by incorporating the rate of angle change, where its benefit has been demonstrated in [10], [15]. Second, other approximation approaches can be studied by resorting to data-driven methods [34], [35]. The Gaussian process will be investigated and compared to the Kalman filters. Third, the current work focuses on the free-bending of the soft actuator, while the sensor deformation may not be the arc shape under the external force. The parameters to describe the shape will be redefined, and the shape deformation model will be studied for a general practical application without the continuous curvature hypothesis.

References

[1] T. Wallin, J. Pikul, and R. Shepherd, "3D printing of soft robotic systems," *Nature Rev. Mater.*, vol. 3, no. 6, pp. 84–100, 2018.

[2] S. Joshi and J. Paik, "Multi-DoF force characterization of soft actuators," *IEEE Robot. Automat. Lett.*, vol. 4, no. 4, pp. 3679–3686, Oct. 2019.

[3] Q. Ji, X. Zhang, M. Chen, X. V. Wang, L. Wang, and L. Feng, "Design and closed loop control of a 3D printed soft actuator," in *Proc. IEEE 16th Int. Conf. Automat. Sci. Eng.*, 2020, pp. 842–848.

[4] G. Gerboni, A. Diodato, G. Ciuti, M. Cianchetti, and A. Menciassi, "Feedback control of soft robot actuators via commercial flex bend sensors," *IEEE/ASME Trans. Mechatronics*, vol. 22, no. 4, pp. 1881–1888, Aug. 2017.

[5] Y. L. Yap, S. L. Sing, and W. Y. Yeong, "A review of 3D printing processes and materials for soft robotics," *Rapid Prototyping J.*, vol. 26, no. 8, pp. 1345–1361, 2020.

[6] K. Elgeneidy, G. Neumann, M. Jackson, and N. Lohse, "Directly printable flexible strain sensors for bending and contact feedback of soft actuators," *Front. Robot. AI*, vol. 5, p. 2, 2018.

[7] T. Hainsworth, L. Smith, S. Alexander, and R. MacCurdy, "A fabrication free, 3D printed, multi-material, self-sensing soft actuator," *IEEE Robot. Automat. Lett.*, vol. 5, no. 3, pp. 4118–4125, Jul. 2020.

[8] G.-Y. Gu, L.-M. Zhu, and C.-Y. Su, "Modeling and compensation of asymmetric hysteresis nonlinearity for piezoceramic actuators with a modified Prandtl–Ishlinskii model," *IEEE Trans. Ind. Electron.*, vol. 61, no. 3, pp. 1583–1595, Mar. 2014.

[9] Y.-R. Ko, Y. Hwang, M. Chae, and T.-H. Kim, "Direct identification of generalized Prandtl–Ishlinskii model inversion for asymmetric hysteresis compensation," *ISA Trans.*, vol. 70, pp. 209–218, 2017.

[10] A. Oliveri, M. Maselli, M. Lodi, M. Storace, and M. Cianchetti, "Model-based compensation of rate-dependent hysteresis in a piezoresistive strain sensor," *IEEE Trans. Ind. Electron.*, vol. 66, no. 10, pp. 8205–8213, Oct. 2019.

[11] J. Zou and G. Gu, "High-precision tracking control of a soft dielectric elastomer actuator with inverse viscoelastic hysteresis compensation," *IEEE/ASME Trans. Mechatron.*, vol. 24, no. 1, pp. 36–44, Feb. 2019.

[12] J. Jansson and M. Sjöberg, "Closed-loop control of a 3D printed soft actuator with soft position sensors," M.S. thesis, KTH Royal Inst. Technol., Stockholm, Sweden, 2021.

[13] D. Habineza, M. Rakotondrabe, and Y. Le Gorrec, "Bouc–Wen modeling and feedforward control of multivariable hysteresis in piezoelectric systems: Application to a 3-DoF piezotube scanner," *IEEE Trans. Control Syst. Technol.*, vol. 23, no. 5, pp. 1797–1806, Sep. 2015.

[14] P. Chen, X.-X. Bai, L.-J. Qian, and S.-B. Choi, "An approach for hysteresis modeling based on shape function and memory mechanism," *IEEE/ASME Trans. Mechatronics*, vol. 23, no. 3, pp. 1270–1278, Jun. 2018.

[15] X. Luo, M. Xiao, Y. Ding, and H. Ding, "Hysteresis modeling and compensation of a pneumatic end-effector based on Gaussian process regression," *Sensors Actuators A: Phys.*, vol. 315, 2020, Art. no. 112227.

[16] X. Tan and J. S. Baras, "Adaptive identification and control of hysteresis in smart materials," *IEEE Trans. Autom. control*, vol. 50, no. 6, pp. 827–839, Jun. 2005.

[17] G.-Y. Gu, C.-X. Li, L.-M. Zhu, and C.-Y. Su, "Modeling and identification of piezoelectric-actuated stages cascading hysteresis nonlinearity with linear dynamics," *IEEE/ASME Trans. Mechatron.*, vol. 21, no. 3, pp. 1792–1797, Jun. 2016.

[18] I. D. Mayergoyz, *Mathematical Models of Hysteresis and Their Applications*. New York, NY, USA: Academic Press, 2003.

[19] Y.-D. Tao, H.-X. Li, and L.-M. Zhu, "Rate-dependent hysteresis modeling and compensation of piezoelectric actuators using gaussian process," *Sensors Actuators A: Phys.*, vol. 295, pp. 357–365, 2019.

[20] G. Wang and G. Chen, "Identification of piezoelectric hysteresis by a novel Duhem model based neural network," *Sensors Actuators A: Phys.*, vol. 264, pp. 282–288, 2017.

[21] C.-H. Chan and G. Liu, "Hysteresis identification and compensation using a genetic algorithm with adaptive search space," *Mechatronics*, vol. 17, no. 7, pp. 391–402, 2007.

[22] L. Liu, K. K. Tan, C. S. Teo, S.-L. Chen, and T. H. Lee, "Development of an approach toward comprehensive identification of hysteretic dynamics in piezoelectric actuators," *IEEE Trans. Control Syst. Technol.*, vol. 21, no. 5, pp. 1834–1845, Sep. 2013.

[23] M.-J. Yang, G.-Y. Gu, and L.-M. Zhu, "Parameter identification of the generalized Prandtl–Ishlinskii model for piezoelectric actuators using modified particle swarm optimization," *Sensors Actuators A: Phys.*, vol. 189, pp. 254–265, 2013.

[24] E. Brekke and M. Chitre, "A multi-hypothesis solution to data association for the two-frame SLAM problem," *Int. J. Robot. Res.*, vol. 34, no. 1, pp. 43–63, 2015.

[25] E. Bayramoglu and O. Ravn, "A novel hypothesis splitting method implementation for multi-hypothesis filters," in *Proc. IEEE 10th Int. Conf. Control Automat.*, 2013, pp. 574–579.

[26] A. Chakraborty, K. Brink, R. Sharma, and L. Sahawneh, "Relative pose estimation using range-only measurements with large initial uncertainty," in *Proc. IEEE Annu. Amer. Control Conf.*, 2018, pp. 5055–5061.

[27] K. Zhao, M. Meuter, S. Müller-Schneiders, and J. Pauli, "A novel multi-hypothesis tracking framework for lane recognition," in *Proc. IEEE 17th Int. Conf. Inf. Fusion*, 2014, pp. 1–8.

[28] Q. Zhang, W. Xu, W. Zhang, J. Feng, and Z. Chen, "Multi-hypothesis square-root cubature Kalman particle filter for speaker tracking in noisy and reverberant environments," *IEEE/ACM Trans. Audio, Speech, Lang. Process.*, vol. 28, pp. 1183–1197, Mar. 2020.

[29] C. Tawk and G. Alici, "Finite element modeling in the design process of 3D printed pneumatic soft actuators and sensors," *Robotics*, vol. 9, no. 3, p. 52, 2020.

[30] K. Elgeneidy, N. Lohse, and M. Jackson, "Bending angle prediction and control of soft pneumatic actuators with embedded flex sensors–a data-driven approach," *Mechatronics*, vol. 50, pp. 234–247, 2018.

[31] K. Ohtani, "Bootstrapping R2 and adjusted R2 in regression analysis," *Econ. Modelling*, vol. 17, no. 4, pp. 473–483, 2000.

[32] B. A. Shenoi, *Introduction to Digital Signal Processing and Filter Design*. Hoboken, NJ, USA: Wiley, 2005.

[33] S. Thrun, "Probabilistic robotics," *Commun. ACM*, vol. 45, no. 3, pp. 52–57, 2002.

[34] G. Fang *et al.*, "Vision-based online learning kinematic control for soft robots using local Gaussian process regression," *IEEE Robot. Automat. Lett.*, vol. 4, no. 2, pp. 1194–1201, Apr. 2019.

[35] Z. Q. Tang, H. L. Heung, K. Y. Tong, and Z. Li, "A probabilistic model-based online learning optimal control algorithm for soft pneumatic actuators," *IEEE Robot. Automat. Lett.*, vol. 5, no. 2, pp. 1437–1444, Apr. 2020.